Controlled Flow Dynamics in a Serpentine Diffuser with a Cowl Inlet

Travis J. Burrows,[1] Bojan Vukasinovic[2] and Ari Glezer[3]
Georgia Institute of Technology, Atlanta, Georgia, 30332-0405

Matthew T. Lakebrink[4] and Mori Mani[5]
Boeing Research & Technology, St. Louis, Missouri, 63042

Pressure losses and distortion in a serpentine diffuser with a cowl inlet are investigated experimentally and numerically over a range of flow rates (Mach numbers at aerodynamic interface plane M_{AIP} of up to 0.6). The present investigations show that in the presence of the cowl inlet the diffuser flow is dominated by two pairs of counter-rotating streamwise vortices that are formed at the sharp edges of the inlet cowl lip. The subsequent evolution and unsteady interactions of these vortices result in significant instantaneous pressure losses that are coupled with high flow distortion at the AIP (remarkably, owing to the flow unsteadiness, the time-averaged distortion is nearly negligible). These losses and flow distortions are strongly mitigated by deliberately drawing ambient air across the cowl surface to form jets that interact with the cowl flow along the its inner surface. The jets are formed through spanwise slots across the cowl's surface by exploiting the pressure difference effected by the cowl flow. The interaction of these jets with the cowl flow alters the formation and evolution of the streamwise vortices and appears to suppress their interactions and thereby significantly diminish the losses and distortion across the full operating range of the diffuser. For example, at $M_{AIP} = 0.5$, the total pressure recovery increases by 8% while the peak circumferential distortion decreases by 35%. The time-averaged circumferential distortion can be further reduced (nearly halved) by using concomitant active flow control at the second diffuser turn.

Nomenclature

AIP	aerodynamic interface plane
C_q	actuation jet mass flow rate coefficient
D	diffuser AIP diameter
DC60	engine-face distortion descriptor
DPCP	SAE circumferential distortion descriptor
$DPCP_{avg}$	average SAE circumferential distortion descriptor
f	frequency
H	diffuser inlet height
L	diffuser length
M_{AIP}	AIP Mach number
M_t	throat Mach number
n	number of flow control jets
p_{ref}	diffuser reference pressure
p_t	total pressure
W	diffuser throat width

[1] Graduate Research Assistant, AIAA Member.
[2] Research Engineer, AIAA Member.
[3] Professor, AIAA Fellow.
[4] Aerodynamics Engineer, AIAA Senior Member.
[5] Boeing Senior Technical Fellow, AIAA Associate Fellow.

I. Introduction

Inlet systems of future fighter aircraft will use embedded engines and more compact, three-dimensionally offset inlet-airframe integration to attain a small spot factor and aerodynamic efficiency. Such inlet systems utilize complex serpentine diffusers that present flow-management challenges, effected by the development of large-scale vortices and boundary-layer separation coupled to throat shocks and aggressive diffuser turns. This secondary-flow phenomenon results in reduced total-pressure recovery and increased flow distortion at the engine face, which can be detrimental to engine operability and performance, but could be mitigated with the implementation of flow-control technology.

Poor performance of supersonic inlets in low speed conditions has been a known issue for decades. The crux of the issue is described well by Henne [1]: "High speed cruise favors thin inlet lips to keep the inlet mass flow ratio high and to keep the nacelle size and, therefore, drag as small as possible. However, high performance at low speed conditions, such as zero forward speed with crosswind and low forward speed with high angle of attack, favors thick inlet lips to efficiently turn the flow into the inlet." The effect of a sharp lip in low-speed air flow was theoretically characterized by Fradenburgh and Wyatt in 1954 [2] using momentum balance analysis on a cylindrical inlet at subsonic free-stream Mach numbers. With this analysis they estimated total-pressure recovery as a function of freestream and inlet Mach numbers. At lower freestream Mach numbers, and especially in the case of zero freestream Mach number, the total pressure recovery plummets, greatly reducing aircraft engine performance. A supersonic inlet model was tested experimentally and found results in reasonable agreement to the theory. Lower pressure recovery means that if an aircraft needs to operate at that condition, it will need a larger engine, increasing the weight and size of the aircraft.

Aircraft that require high performance in both low-speed and high-speed conditions need a variable geometry inlet. The vertical and/or short take-off and landing (V/STOL) fighter type aircraft were among the first to encounter this issue, because they must both hover (high inlet speed, zero free-stream Mach number) and cruise at a high speed. In the 1960s, during the development of the prototype Hawker P1127 V/STOL aircraft, an inflatable lip was designed and tested [3]. The idea was to inflate a rubber balloon on the lip to approximate a bell-mouth during low-speed operation and deflate it to create a sharp lip for high-speed operation. After testing, this solution was determined to be not feasible because the rubber would ripple and tear at high speeds.

The auxiliary inlet with passive flaps known as blow-in doors were ultimately chosen and implemented on Harrier production aircraft [4]. An auxiliary inlet is a bell-mouth-like slot going around the circumference of the primary inlet increases the inlet area and enables some mass flow to bypass the sharp lip leading to higher pressure recovery. The blow-in doors are hinged covers for the slots that open when the pressure is lower within the inlet (at low-speed operation) and remain shut when the opposite is true (at high-speed operation). Similar blow-in covers for low speed operation were used on the Boeing 707, 737-200, and 747, on the B-52, and MiG-29 [5], and to provide extra stall margin during takeoff and landing on General Dynamics' YF-16 [6]. Powell et al. [7] conducted tests of variable cowl slots on an axisymmetric mixed-compression supersonic inlet in 1985 at free stream Mach numbers of 0, 0.1, and 0.2. They reported that at low speeds the slot reduced flow separation associated with the sharp lip as well as improve the total pressure recovery and time-averaged distortion. Garzon [8] used CFD simulations to investigate the benefits of integrating a translating cowl on a supersonic business jet to improve low speed performance at free stream Mach number of 0.1 and reported that while the pressure recovery was improved, pressure distortion increased and was attributed to the positioning of the boundary-layer diverter, which changed the pattern of incoming flow.

The present coupled experimental/numerical investigations focus on assessment of pressure losses and distortion in a serpentine diffuser integrated with a cowl inlet that is suitable for high-speed flight during low-speed (takeoff) operation. Specific attention is paid to the cowl-induced streamwise counter-rotating vortices whose unsteady interactions dominate the flow within the diffuser and lead to significant instantaneous pressure losses and flow distortion. It is shown that the formation and evolution of the streamwise vortices and their detrimental effects on the flow can be substantially altered by jets of air that is drawn by the pressure differences across the cowl.

II. Experimental Setup and Flow Diagnostics

The present experiments are performed in an open-return, pull-down, high-speed subsonic wind tunnel driven by a 150 hp blower in which the temperature of the return air is controlled using a chiller, coupled with an ultra-low pressure drop heat exchanger (Figure 1). An aggressive offset diffuser model having a cowl inlet (Figure 1b) is installed in the tunnel and a ground plane at the cowl's inlet emulates the effect of an adjacent aerodynamic surface. Downstream, of the cowl, the diffuser has a D-shaped inlet and a round aerodynamic interface plane (AIP) with diameter, $D = D_{AIP} = 0.127$ m. The offset between the throat and AIP is $0.4 \cdot D$, length-to-diameter ratio $L/D = 3.7$, throat width $W/D = 1.78$, and height $H/D = 0.48$.

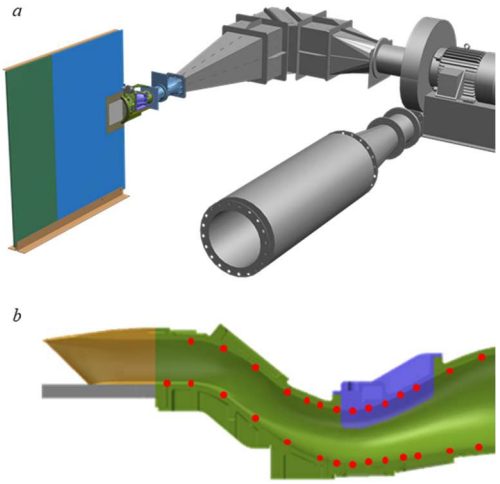

Figure 1. *CAD model of pull-down wind tunnel facility with flat-plate approach-flow geometry (a), and section view of the diffuser (b) with pressure ports marked in red.*

The total steady and dynamic pressures at the AIP are measured using a 40-probe array arranged in eight, equiangularly spaced rakes around the circumference of the AIP according to the SAE industry standard ARP1420b (rake provided by the Boeing Co.). Each probe comprises of a miniature high-frequency pressure transducer (Kulite) that enables simultaneous sampling frequencies up to 50 kHz enabling spectral analysis of the total pressure field (in the present experiments, the 40 transducers were sampled simultaneously at 25 kHz over a 10 second interval) and a total pressure tube yielding the local time-averaged pressure. Each of the eight radial 5-probe rakes is matched with a corresponding azimuthal opposite static pressure port on the inner surface of the diffuser. In addition, fifteen static pressure ports are distributed along each of the inner bottom and top surfaces of the diffuser wall (cf. Figure 1). Time-averaged static and total pressures are measured using a pressure scanner (PSI Netscanner) system using 100 sets of 64 independent samples. The estimated uncertainties of the mean pressures and of the derived $DPCP_{avg}$ parameter are less than 1 and 2%, respectively.

In the present experiments, the flow within the cowl and the diffuser is controlled using arrays of spanwise slots on the surface of the cowl (Figure 2), and an array of fluidic oscillating jets at the diffuser's second turn. As noted in §I, the streamwise vortices that are formed by the baseline cowl are manipulated using spanwise slots along the surface of the cowl that guide ambient air driven by the pressure difference through the surface and form transverse jets along the cowl's inner surface. Three bleed slots across the cowl's outer surface are shown in Figure 2. Pressure losses through the slots are minimized by contouring the surfaces at their inlets and outlets. Although in the present investigations the bleed slots are kept open, it is noted that the slots can be equipped with actuated louvers for regulating the bleed flow. In addition, flow actuation at the diffuser's second turn is provided by a spanwise array of 13 equally-spaced (6.3 mm apart) fluidic oscillating jets (cf. Burrows et al., [9]). Each jet orifice measures 1.5 × 2 mm, with an operating frequency $7 < f < 9$ kHz (decoupled from internal diffuser flow instabilities over the present range). In the present experiments the mass flow rate coefficient of the array $C_q < 0.5\%$.

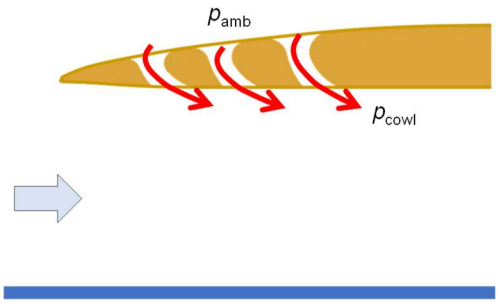

Figure 2. *Cross section of three streamwise-successive spanwise air bleed slots directing ambient air into the cowl flow.*

III. Numerical Approach

For the numerical investigation, second-order-accurate solutions to the compressible Navier-Stokes equations were obtained using the Boeing Computational Fluid Dynamic (BCFD) finite-volume flow solver [10]. BCFD supports continuum-gas simulations of general-geometry structured and unstructured grids, for flows ranging from low subsonic to hypersonic. An extensive array of boundary conditions, numerical schemes, turbulence models, and gas models are available within BCFD for both steady-state and time-accurate simulations. In steady-state simulations, first-order implicit time integration is performed, and local eigenvalues are used to obtain a spatially varying time-step and accelerate convergence. For time-accurate simulations, a dual-time approach is used to obtain second-order temporal accuracy.

The simulations conducted for the present study assumed calorically perfect air with constant laminar and turbulent Prandtl numbers of 0.72 and 0.90, respectively. Viscosity was computed using Sutherland's law. Solid boundaries were modeled as no-slip adiabatic walls, total pressure and total temperature were prescribed on the inflow boundary, and a uniform pressure was prescribed on the outflow boundary to achieve the desired flow rate. Delayed Detached Eddy Simulations (DDES [11]) were conducted using Spalart-Allmaras [12] with rotation correction [13] and the

quadratic constitutive relation (SA-RC-QCR) [14] . Bounded central differencing [15] was employed to reduce numerical dissipation and improve resolution of turbulent eddies.

The computational domain used for CFD analysis incorporates key components of the wind tunnel at Georgia Tech, including the contraction, flow-control elements, and AIP-instrumentation housing. An unstructured surface grid consisting of triangular elements was created using the Modular Aerodynamic Design Computational Analysis Process (MADCAP). A volumetric grid comprising prisms, pyramids, and tetrahedra was then constructed using the Advancing Front Local Reconnection (AFLR [16]) software. Anisotropic triangular prisms were used to resolve the boundary layer. An initial normal spacing of 2.5 μm was held constant for three layers away from the boundary. The growth rate for the normal spacing grew from 1.05 at layer four, to a maximum value of 1.10. A grid-resolution study was performed to reduce discretization error and the following best practices were established. Surface-element sizes throughout the diffuser were nominally 0.05 mm. Surface elements along the cowl leading edge were nominally 0.025 mm. Background Cartesian grids were used to enforce the size of tetrahedral elements outside of the prism layer to be no greater than 1.27 mm, and the final mesh consisted of nominally 140-million elements for the baseline cowl, and 150-million elements for the slotted cowl.

Corrected mass flow rates ranging from 1.36 to 2.27 kg/s through the diffuser were considered. Baseline-flow comparison between CFD simulations and experimental data showed that steady-state Reynolds-Averaged Navier-Stokes (RANS) was unable to accurately predict key flow features in the diffuser flow, particularly evolution of cowl vortices between throat and AIP. To address this inadequacy, time-accurate Delayed Detached Eddy Simulations (DDES), aided by the low-dissipation bounded central differencing technique, were performed. The time step used for time-accurate simulations was chosen, based on characteristic velocity and cell size, to be 4e-6 seconds.

IV. The Base Flow

The main structural features of the base flow are characterized using spatial distributions of the time-averaged vorticity concentrations and corresponding distributions of the total pressure in successive streamwise cross sections of the diffuser that are produced by the numerical simulations, as shown in Figures 3a and b, respectively. These data show that in the presence of the cowl, the diffuser flow is dominated by four primary streamwise vortices including a center counterrotating vortex pair that forms at the cowl's central edges and single opposite sense vortices that are each formed at the cowl's corners. The center counter-rotating vortex pair begins to move away from the top surface ostensibly under their own self-induced velocity field downstream of the diffuser's throat and by the time they reach the second turn they appear to be located closer to the centerline. However, at this position the time-averaged vortices appear to be weaker and radially diffused, an indication of temporal unsteadiness until they all but vanish at the AIP. In contrast, the corner vortices which are anchored by the diffuser's corners are still present at the AIP, albeit significantly weaker. The losses effected by the presence of the streamwise vortices are illustrated by cross-sectional distributions of the total pressure (Figure 3b). The flow domains about the cores of these vortices are characterized by lower total pressure as a result of the advection and entrainment of low-momentum fluid from the top surface of the cowl by the center pair and from the flow periphery around each of the corners. The concentrated pressure losses associated with the center pair begin to diffuse downstream of the diffuser's throat and spread radially indicating that flow unsteadiness leads to significant mixing such that virtually no signature of these losses remains at the AIP. All the while, the losses at the corners remain more coherent through the AIP.

The evolution of the diffuser flow is represented by static pressure distributions along its lower and upper surfaces as depicted in Figures 4a and b, respectively (the diffuser's throat and its AIP are at x/D = -3.5 and 0, respectively). Distributions of the pressure coefficients $C_P = 2\,(p/p_{\mathrm{ref}} - 1)/\left(1.4\,M_{\mathrm{AIP}}{}^2\right)$ (the static reference pressure p_{ref} is taken

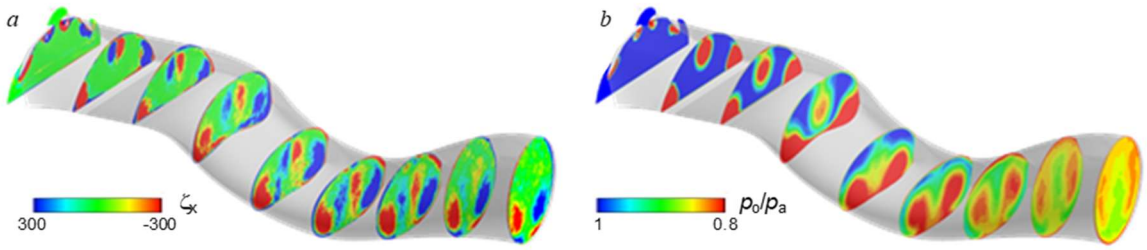

Figure 3. *Color raster plots of concentrations of the streamwise vorticity (a) and distributions of the total pressure (b) in equally spaced streamwise-successive cross sections of the diffuser beginning at x/D = -4.75, at M_{AIP} = 0.5. The inner surface of the diffuser is overlaid in gray for reference.*

at top surface at the AIP) are shown for seven cases between M_{AIP} 0.3 and 0.5. The corresponding pressure distributions from the numerical simulations for M_{AIP} = 0.5 which is overlaid (dotted line) on the experimental data exhibits a good agreement between the simulated and measured flows. As the outer flow enters the cowl, the lower surface pressure (Figure 4a) indicates that the flow begins to accelerate even prior reaching the diffuser throat (x/D = -3.5). The suction peak is reached shortly past the throat, which is followed by the sharp pressure rise. This domain of the sharp adverse pressure gradient is critical from the standpoint of possible local flow separation, however, a small drop in the pressure gradient at x/D = -3.2 is not found to be associated with the flow separation. Thereafter, the pressure increases up to about x/D = -1.6 and then begins to decrease monotonically towards the AIP. The upper surface pressure distribution is clearly more complex as a result of the dominant streamwise vortices (cf. Figure 3a). It is interesting to note that the flow decelerates along the upper surface, immediately downstream of the diffuser's throat, while it accelerates along the lower surface. Following relatively flat extent, the flow sharply accelerates over a short distance, down to x/D = -2.6. Past this point, it exhibits several consecutive accelerations and decelerations before reaching the diffuser second turn (x/D = -1.7), over which it has its final acceleration. Past the second turn, the flow faces a steady adverse pressure gradient from about x/D = -1.7 to just about the AIP plane.

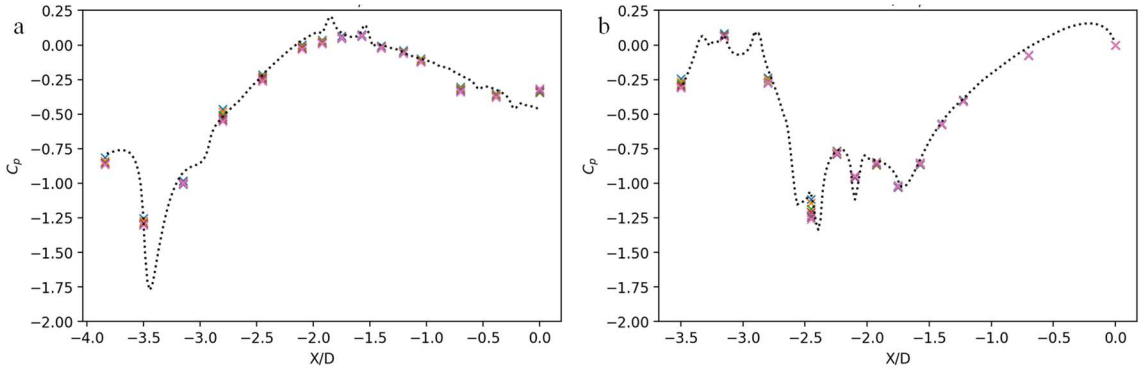

Figure 4. *Streamwise variation of the diffuser centerline pressure in the base flow along the lower (a) and upper (b) surfaces including experimental measurements (M_{AIP} = 0.3, 0.35, 0.4, 0.425, 0.45, 0.475, and 0.5) and numerical results (M_{AIP} = 0.5, dotted line).*

The flow quality at the diffuser's AIP to the engine is assessed from distributions of the total pressure measured by the AIP 40-proble rake (cf. §II). Color raster plots of the time-averaged total pressure at the AIP are shown in Figure 5 for 0.3 < M_{AIP} < 0.5 (cf. Figure 4). A common aspect of all these distributions is the absence of dominant features that would normally indicate the presence of coherent secondary flows (e.g., streamwise vortices) except perhaps a region of somewhat lower pressure along the lower segment of the AIP plane. This is in stark contrast to typical raster plots of the AIP total pressure in the same diffuser in the absence of the cowl that are associated with streamwise vortices that form as a result of flow separation at the diffuser's first and second turns [9]. These raster plots support the observation that the streamwise vortices that form in the presence of the cowl become unstable as

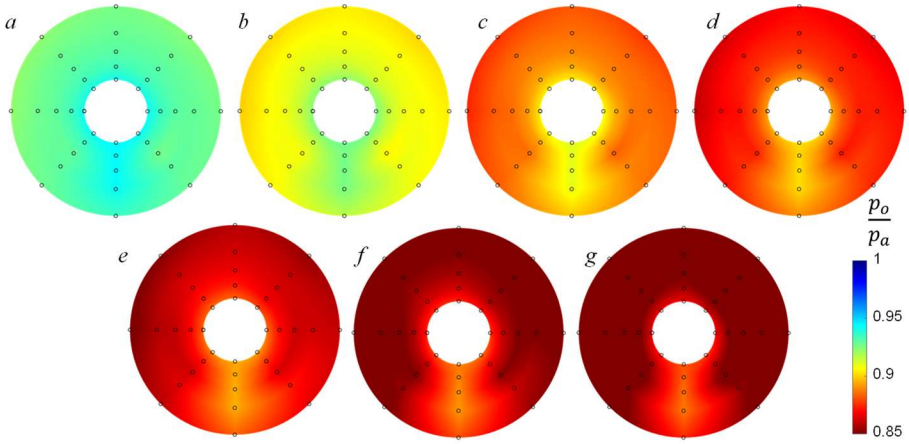

Figure 5. *Color raster plots of the time-averaged total pressure at the AIP for M_{AIP} = 0.3 (a), 0.35 (b), 0.4 (c), 0.425 (d), 0.45 (e), 0.475 (f), and 0.5 (g).*

the flow expands through the diffuser and therefore their time-averaged signature is smeared. This points to the need for the time-resolved total pressure measurements to adequately capture the total pressure variations across the AIP, i.e., the total pressure distortion. The second common feature and another contrasting characteristic relative to the diffuser flow in the absence of cowl is that there is a significant drop in the total pressure magnitude from the diffuser intake to the AIP. Clearly, this drop is proportional to the diffuser Mach number, as seen in Figure 5, and amounts to the loss of about 15% at the highest Mach number (Figure 5g). For comparison, there was only about 4% of the total pressure loss in the integrated diffuser [9], which points to the shift in the flow control objective of these two diffuser flow configurations. While the total pressure distortion was the prevailing drawback of the integrated diffuser flow, diffuser coupled to the cowl generates significant total pressure losses and minimization of the total pressure loss, or improvement of recovery, becomes the main flow control objective.

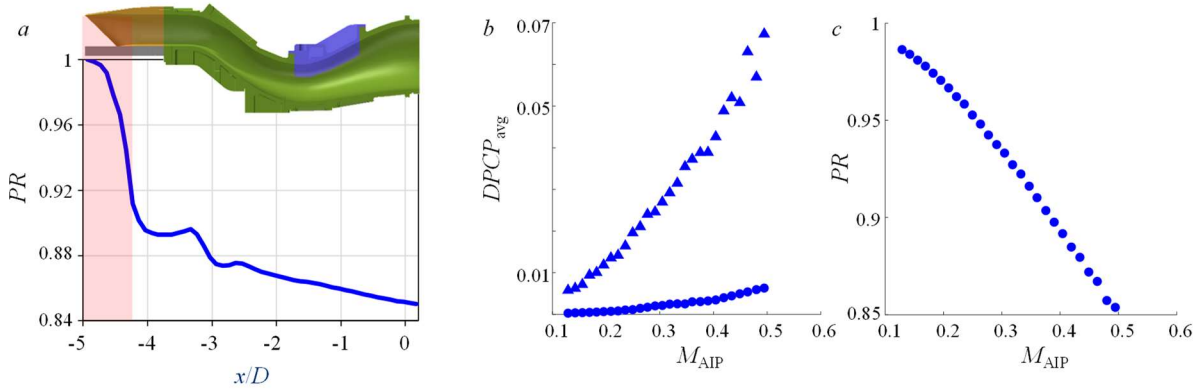

Figure 6. *a) Computed streamwise variation of time-averaged pressure recovery along the diffuser; Variation with the AIP Mach number of (b) Time-averaged (●) and peak (▲) $DPCP_{avg}$ and (c) Total pressure recovery.*

As the cowl coupling is clearly responsible for the dramatic increase in the total pressure loss, this total pressure evolution is more closely examined in Figure 6a through the streamwise evolution of the numerical recovery parameter at $M_{AIP} = 0.5$. For reference, diffuser geometry is overlaid above the plot. There is a dramatic drop of total-pressure recovery within the cowl inlet, which is highlighted in red. Total pressure continues to decrease past that point, but about 73% of the total pressure loss through the diffuser occurs during the flow through the cowl inlet. This finding clearly points to where the flow control needs to be focused in order to suppress losses and improve the flow recovery. As pointed out in discussion of Figure 5, steady-state total pressure distortion is not sufficient to characterize the total pressure nonuniformity at the AIP. Therefore, both the steady-state and time-resolved total pressure measurements are conducted at the AIP with the varying diffuser flow (Mach number). As a representative distortion parameter, face-averaged circumferential distortion parameter $DPCP_{avg}$ is computed for both the instantaneous and time-averaged total pressure fields. Besides the steady-state $DPCP_{avg}$ over the diffuser Mach number range 0.1 – 0.5, Figure 6b shows the peak $DPCP_{avg}$ from the time-resolved total pressure measurements, i.e., the $DPCP_{avg}$ is plotted at the instant in time when this distortion is maximal. Clearly, there is a great disparity between the steady-state distortion parameters and their corresponding peak values. The $DPCP_{avg}$ magnitudes calculated from steady-state total pressures remain low throughout the whole range of Mach numbers (less than 0.007 at $M_{AIP} = 0.5$), due to the relative uniformity and symmetry of the total pressure fields at the AIP, as already seen in Figure 5. When considering the time-resolved distortion parameters, their magnitudes are multi-folds higher than at their steady-state counterparts, reaching even an order of magnitude higher value at the highest Mach number. Besides the huge disparity in magnitudes, there is also a difference in the distortion rate of change with Mach number, where the peak distortion parameter has a much steeper rate of change than the steady state $DPCP_{avg}$ parameter. Similar to the evolution of the steady-state total pressure distortion with M_{AIP} in Figure 6b, the total pressure recovery evolution is shown in Figure 6c. This parameter is the main indicator of the flow losses in this internal flow geometry, and it is seen that decreases nearly-linearly with M_{AIP}, exceeding the 10% loss already at M_{AIP} of about 0.4. As discussed in conjunction with Figure 4, the bulk of these losses incurs over a portion of the flow through the cowl, and any improvement of recovery would have to be sought by addressing the cowl flow.

Another illustration of the effects of flow unsteadiness at the AIP is shown in Figure 7 for $M_{AIP} = 0.5$. The time-averaged total pressure at the AIP in Figure 7a shows that while there is a significant loss of total pressure at the AIP, it is nearly-uniform except at the lower central region that exhibits a slightly lower drop in pressure. Although these magnitudes imply a significant effect on the total pressure recovery, the circumferential distortion is only weakly

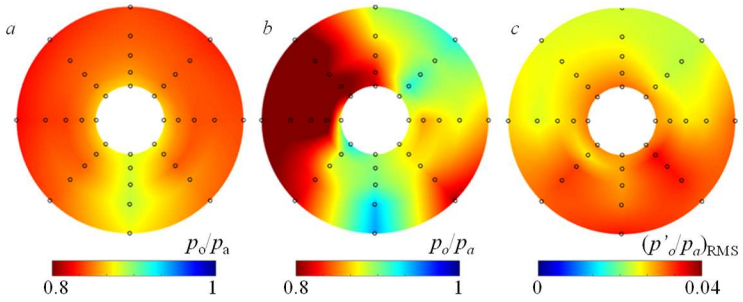

Figure 7. *AIP color raster plots in the diffuser's base flow (M_{AIP} = 0.5): a) Time-averaged total-pressure; b) Total-pressure associated with the peak $DPCP_{avg}$ distortion; and c) Total-pressure RMS.*

increased. As long as there are significant departures from the time-averaged total pressure distributions, they need to be quantified, particularly if the flow is highly unsteady. The interplay among the four dominant streamwise vortices (cf. Figure 3a) certainly introduces significant unsteadiness and it is to be expected that the total pressure distribution across the AIP at any instant in time might significantly depart from the steady state measurement. Indeed, when the instantaneous total pressure distribution is plotted for the instance in time that corresponds to the maximum $DPCP_{avg}$ (Figure 7b), a highly nonuniform distribution is seen, having the most losses associated with one side of the flow. On the face-average, the mean total pressure might not differ much from its counterpart in Figure 7a, but the highly nonuniform distribution drives the high instantaneous circumferential distortion. Lastly, to quantify the level of unsteadiness in the AIP total pressure, a contour plot of the RMS of the total pressure fluctuations is shown in Figure 7c. Although the fluctuation levels are high across the AIP, it is also shown that consistently higher levels of unsteadiness are measured along the lower portion of the AIP.

V. Cowl Inlet Flow Control

Guided by the sharp drop in the total pressure along the inlet section of the cowl (cf. Figure 6a) and an indication that the counter-rotating vortex pair along the upper surface (cf. Figure 3a) creates a stagnation zone upon entering the diffuser (cf. Figure 4b), it is decided that the flow control should focus on disruption of this vortex pair formation along the cowl upper surface. To facilitate this, three autonomous bleed slots are opened across the cowl upper surface, as schematically shown earlier in Figure 2. They utilize the existing pressure difference across the outer air and the inner flow drawn into the diffuser. In principle, these slots can be equipped by louvers and commanded to open and close, but in the present experiments they are kept open at all time for the current proof-of-concept study. The entrance to the slots on the outer side is bell-mouth-like to minimize pressure losses, and on the flow-side they are contoured to guide the airflow smoothly into the cowl, right at the vortex pair formation region, aimed at the vortex disruption, in an effort to bypass the sharp loss in the total pressure in that region (cf. Figure 6a).

The surface pressure profiles in the controlled flow analogous to the base flow profiles of Figure 4 are shown in Figure 8 in terms of the pressure coefficient C_p over the full range of experimental M_{AIP} = 0.3 – 0.5. In addition, numerical results for M_{AIP} = 0.5 are overlaid as a dotted line. Similar to the base flow analysis, a good agreement is obtained between the simulated and measured flows. Both the lower and upper surface pressure profiles in the controlled flow are similar in shape to the corresponding profiles in Figure 4. The main difference along the lower surface is in the higher initial flow acceleration, resulting in the lower suction peak along the diffuser throat area. Although the upper surface central C_p profile (Figure 8b) is also similar in shape to the corresponding base flow profile

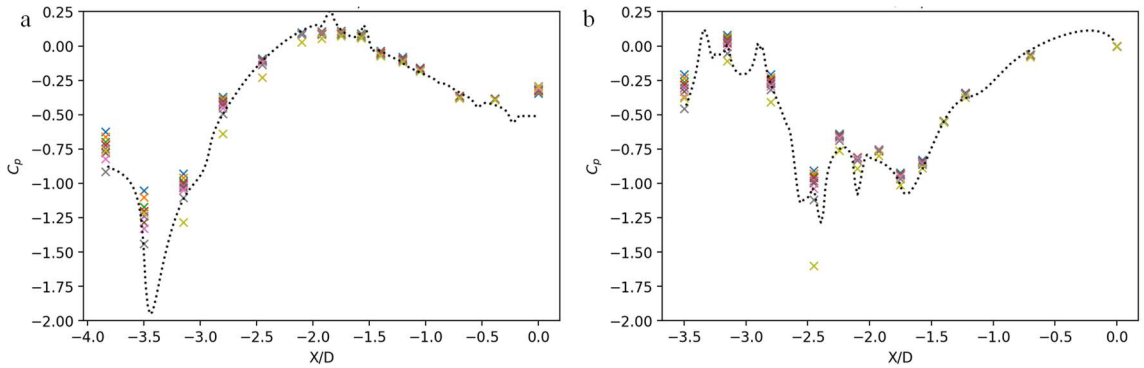

Figure 8. *As in Figure 4, streamwise variation of the diffuser's centerline pressure in the presence of ambient air bleed across the cowl .*

(Figure 4b), there are two domains where the pressure levels deviate. The stagnation region with elevated pressure levels immediately upon the flow entrance into diffuser is mostly lowered in magnitude, indicating the enhanced flow passage. Conversely, flow acceleration around x/D = -2.5 becomes less pronounced in the controlled flow, preceding the successive flow accelerations and decelerations.

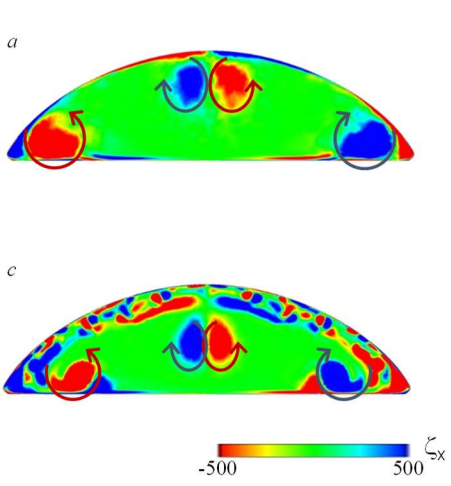

Figure 9. *Color raster plots of the computed time-averaged streamwise vorticity concentrations at the diffuser's throat (x/D = -3.5, a, c) and at the AIP (b, d) for base flow (a, b) and in the presence of ambient air bleed across the cowl (c, d) at M_{AIP} = 0.5.*

As a quick assessment of the autonomous bleed effect on the diffuser flow entering and exiting the diffuser, contour plots of the simulated streamwise vorticity component ζ_x are plotted in Figure 9 at the diffuser throat and AIP, for both the controlled and uncontrolled flow at M_{AIP} = 0.5. The base flow entering the diffuser (Figure 9a) is marked by the four characteristic streamwise vortices: a corner vortex in each corner of the D-shaped throat, and the counter-rotating vortex pair centered along the upper surface of the throat. As it can be expected, each of the vortices also pulls a different sense of vorticity off of the bordering surface. Several important distinctions are seen in the flow entering the diffuser past the cowl that is controlled by the autonomous bleed (Figure 9c). First, the flow drawn through the bleed slots generates small-scale vortical concentrations, which subsequent interaction and breakup lead to the increased flow mixing. Perhaps even more significant impact of the flow control is seen in the displacement of the counter-rotating vortex pair away from the surface, which is expected to have a major effect on the total pressure losses. Additionally, it should be noted the countering sense of vorticity generated in the corners, which not only weakens the corner-formed vortices, but also displaces them away from the corners, along the bottom surface. As for the flow difference at the AIP (Figure 9b and d), there is not much difference in the vortical structure along the bottom surface, except for the size and extent of the vortical structures. Both vortices at the AIP in the controlled flow are significantly diminished in size, although advanced slightly closer to each other. The other interesting feature of the controlled flow is the appearance of a small pair of counter-rotating vortices along the upper surface that are not present in the base flow.

To illustrate how the cowl flow control ultimately affects the flow global structure at the AIP, Figure 10 shows the total pressure contour plots for the AIP Mach numbers 0.3, 0.4, 0.5, and 0.6 (Figure 10a-d). First, and arguably the most important difference when comparing Figures 10a–c to their base flow counterparts shown in Figures 5a,c,g is the elevated total pressure magnitude across the whole AIP face. This is a clear indication that the applied flow control has a significant effect on the total pressure losses through the diffuser. Second, although the total pressure contour at M_{AIP} = 0.3 (Figure 10a) appears nearly featureless, some interesting features appear at the higher Mach numbers (Figures 10b and c). Accumulation of the total pressure deficit is seen over the central top surface, much like in the case of an integrated diffuser [9]. In addition, more isolated regions of reduced total pressure appear across the AIP face, but all of them are of a relatively small deficit magnitude. Lastly, as a consequence of the reduced losses, the controlled diffuser flow is capable of drawing the higher flow rate, which is depicted through the additional AIP

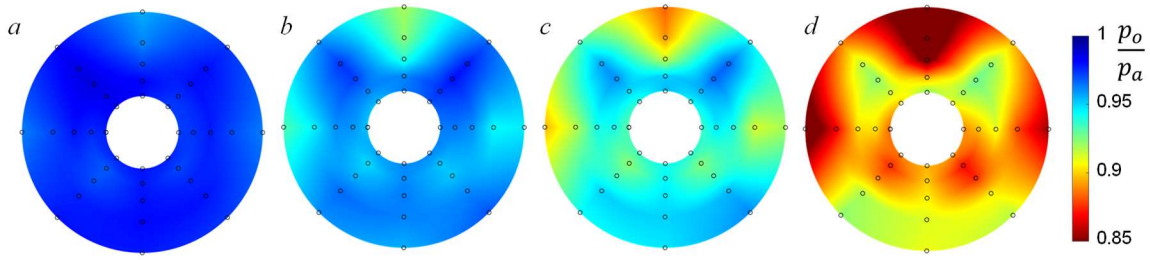

Figure 10. *Color raster plots of the time-averaged total pressure distribution at the AIP for M_{AIP} = 0.3 (a), 0.4 (b), 0.5 (c), and 0.6 (d) in the presence of ambient air bleed across the cowl.*

contour shown in Figure 10d for M_{AIP} = 0.6. In contrast, the uncontrolled diffuser can draw the flow up to just over M_{AIP} = 0.5 before reaching the blower limit.

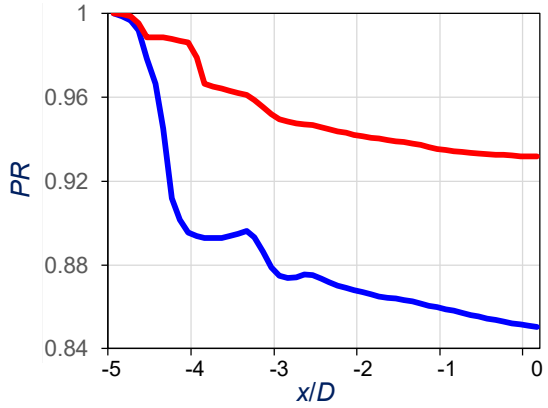

Figure 11. *Computed streamwise variation of the total pressure recovery (PR) along the diffuser for the base flow (—) and in the presence of ambient air bleed across the cowl (—) for M_{AIP} = 0.5.*

As an integral measure of the total pressure losses, distributions of the cross-sectional total pressure averages along the diffuser, i.e., the total pressure recovery, are shown in Figure 11 for the base and controlled flows at M_{AIP} = 0.5. As the outer flow is captured by the cowl, both flows enter the flow geometry with no losses in the total pressure and hence have recovery of 1. Both flows exhibit about the same loss in recovery up to the first slot for autonomous bleed in the controlled flow. The following sharp drop in recovery of the base flow becomes fully mitigated by the autonomous bleed, which maintains almost invariant recovery over the streamwise extents of the bleed. It should be noted that the bleed flow does not only affect the vortex formation and interaction but also add the mass flow rate, such that only downstream from the last bleed slot there is diffuser mass flow rate equivalent to that of the base flow diffuser, i.e., in the absence of flow control. This established equivalent flow rate is marked by a notable drop in recovery immediately downstream from about x/D = -4. Similar local drop in recovery of the base flow is seen just as the flow turns about the first diffuser bend, starting at about x/D = -3.3. Interestingly, the local loss in recovery in the controlled flow becomes also suppressed even about the first diffuser turn. For the remaining flow downstream from the first turn, there is not just the difference in the absolute levels of recovery, but the controlled flow remains to incur less losses of total pressure, as the recovery decreases as lower rate than in the base flow. Overall, the flow control effects a great increase in recovery, up to 93% from 85% across the whole diffuser.

The numerical simulations provide detailed insight into the effected structural modifications of the diffuser flow that are brought about by ambient air bleed across the cowl surface and lead to the flow changes at the AIP. Similar to Figure 3, these structural features are characterized using distributions of the time-averaged vorticity and total pressure in successive streamwise cross sections of the diffuser are shown, respectively in Figures 12a, b and c, d for the base and modified cowl flows (the data from Figures 3a and b are repeated for reference in Figures 12a and b). These data clearly reflect the effects of the cowl bleed on the dominant streamwise vortices. As shown in Figure 12c, the autonomous cowl bleed forms a layer of small-scale vorticity concentrations (relative to the dominant vortices), that, as discussed in connection with Figure 9c, result in vertical and horizontal displacements of the central vortex

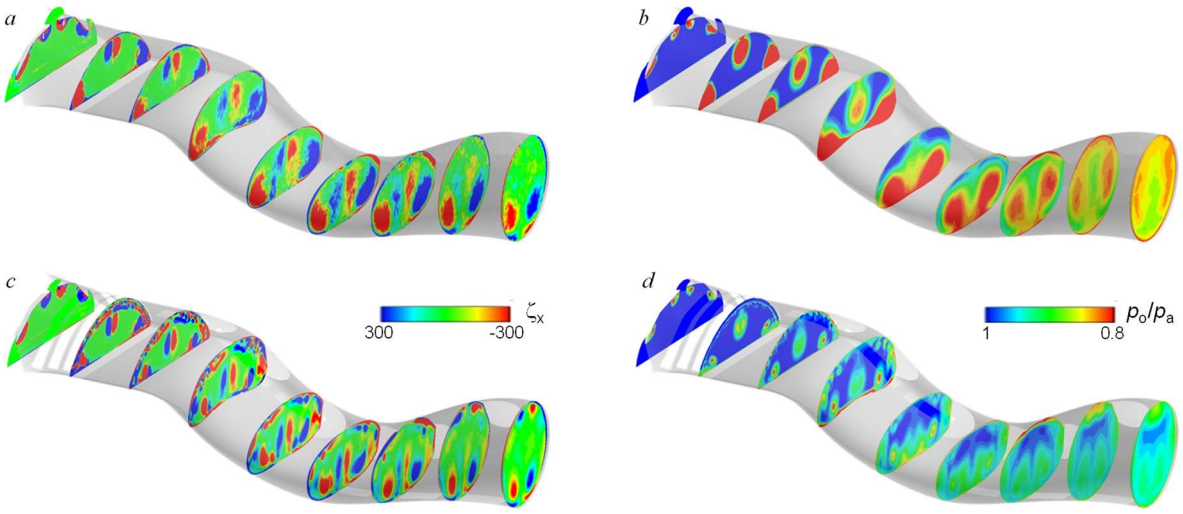

Figure 12. *As in Figure 3, computed concentrations of streamwise vorticity (a, c) and distributions of the total pressure (b, d) in streamwise-successive cross sections of the diffuser for the base flow (a, b) and in the presence of ambient air bleed across the cowl (c, d) at M_{AIP} = 0.5.*

pair and the corner vortices, respectively that are somewhat larger than in the corresponding base flow. It is noteworthy that unlike the base flow, the cowl bleed leads to the formation of two pairs of counter-rotating streamwise vortices along the top and bottom surfaces of the AIP. The sectional total pressure distributions plots along the diffuser in Figure 12d exhibit significantly lower levels of the total pressure deficit including the vortex cores (although the highest deficit initially is still associated with the vortex cores, the total pressure levels are higher than in the base flow), and ultimately the total pressure level at the AIP is significantly higher than in the presence of cowl bleed.

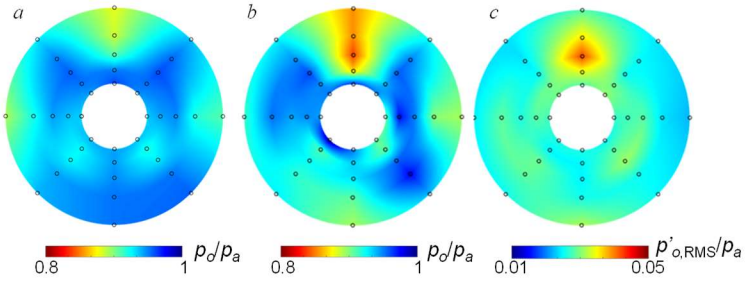

Figure 13. *AIP color raster plots in the presence of ambient air bleed across the cowl (M_{AIP} = 0.5): (a) Time-averaged total-pressure; (b) Total-pressure associated with peak $DPCP_{avg}$ distortion and (c) Total-pressure RMS.*

Analysis of the flow control effectiveness has focused on the steady-state, or the time-invariant measures. A direct comparison of both the steady and time-resolved critical flow characteristics at the AIP to the cases shown in Figure 7 for the base flow are shown in Figure 13. Steady-state total pressure contour plot in Figure 13a indicates much higher overall total pressure magnitude than in the base flow (Figure 7a). Besides this main difference, it is also notable that there is a higher nonuniformity of the total pressure across the AIP in the controlled flow. In particular, as already emphasized earlier, a new domain of lowered total pressure has developed along the central upper surface. Still, the overall total pressure deviation across the AIP remains relatively low, albeit increased from the base flow. Even greater difference between the controlled and the base flow is observed when comparing the total pressure distributions across the AIP at the maximum circumferential distortion in the time-resolved measurements of the controlled flow (Figure 13b). When compared to its base-flow counterpart (Figure 7b), it is seen that the overall drop in the total pressure across the AIP is much less pronounced. Also, the total pressure excursions are much milder than in the base flow. Another interesting point is that there is no big difference in terms of the total pressure shape in the steady-state case (Figure 13a) and at this peak distortion, which may point to the lower unsteadiness in the controlled flow. Indeed, when the RMS of the total pressure fluctuations is plotted (Figure 13 c), the same trend in comparisons to the base flow (Figure 7c) still holds – there is much lower level of the unsteadiness across the whole AIP face. It is interesting to note that the only domain of the elevated fluctuations of the total pressure is associated with the newly-formed upper domain of the total pressure deficit, which is argued to be associated with the two counter-rotating vortices shown earlier (e.g., Figure 9d).

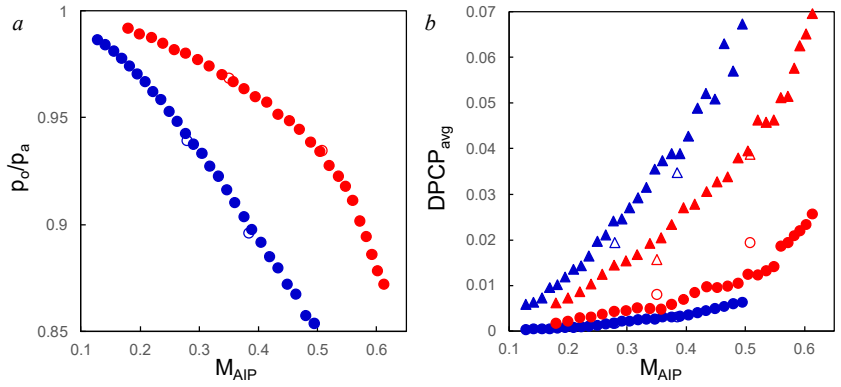

Figure 14. *Measured variation with AIP Mach number of: a) Total pressure recovery; and b) time-averaged (●) and peak (▲) $DPCP_{avg}$ in the **base** and **controlled** cowl flows. The numerical results are shown using open symbols.*

Evolution of the main flow parameters over the full range of the diffuser mass flow rates is shown in Figure 14 for both the uncontrolled and controlled flows. As already assessed on one characteristic flow condition (M_{AIP} = 0.5) above, there is a notable increase in the total pressure recovery across the full range of the diffuser Mach numbers (Figure 14a). While the base flow recovery decreases in a nearly linear fashion, it is seen that the controlled flow recovery initially decreases at the lower rate with the increase in M_{AIP}, up to about M_{AIP} = 0.5. Its slope changes for the highest diffuser flow rates, and it appears that the recovery decreases thereafter at the rate comparable to the base flow. Consequently, the relative improvement in recovery is lowest at the lowest Mach numbers and then progressively increases with the increasing Mach number up to about M_{AIP} = 0.5. In addition to the detailed experimental measurements, two of the simulated conditions are also included in the plot in open symbols, where an excellent agreement with experimental measurements is noted. It should be noted that an alternative view of the achieved increase in recovery would be

stated in terms of the enabled higher flow rates through the diffuser. As the diffuser flow is capable achieving M_{AIP} = 0.6 with the flow control, compared to the limit of about M_{AIP} = 0.5 in the uncontrolled flow (both are facility blower limited), it can be argued that from the aircraft perspective, the flow control would enable much more thrust. To assess the changes in the steady-state and time-resolved circumferential distortion, these parameters are extracted from the same sequence of the experimental measurements used for the recovery calculations, and the results are shown in Figure 14b, again with addition of the two sets of results obtained from the corresponding numerical simulations. Just like in the case of the recovery analysis, the previous conclusions based on the single flow condition of M_{AIP} = 0.5 are confirmed over the full range of the diffuser Mach numbers. Perhaps not surprisingly, the steady-state distortion somewhat increases in the controlled flow. This is due to a combination of the extremely low distortion levels in the base flow and the steadying of the vortices with autonomous bleed. As already seen in Figure 10, the controlled flows form some total pressure signatures at the AIP, which inevitably lead to the increased distortion levels. Still, the overall levels of distortion remain low in the absolute sense. The main effect of the flow control is seen in the significant lowering of the peak distortion levels, which become reduced by about 35% across the board. This is again in agreement with the previously examined case of M_{AIP} = 0.5 (Figure 13), where the increased overall levels of the total pressure are coupled with suppressed non-uniformities in its distribution across the AIP. The agreement between numerical and experimental results is good, with some deviations in magnitudes, while the trends are captured exactly.

VI. Hybrid Flow Control at the Cowl and the Second Turn

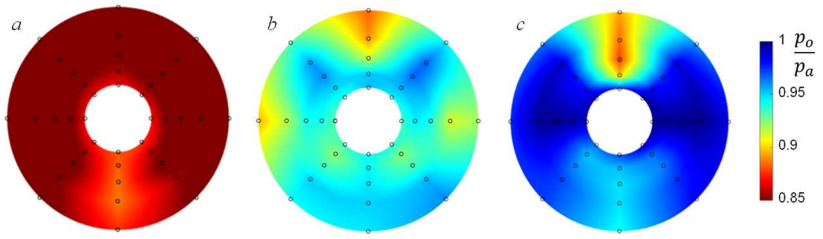

Figure 15. *Color raster plots of the time-averaged total pressure (M_{AIP} = 0.5) for the base flow (a) and in the presence of ambient air bleed across the cowl (b). A corresponding raster plot of the time-averaged total pressure in an isolated diffuser in the absence of an inlet cowl [9] is shown in (c).*

As depicted in Figure 14b, significant decrease in the peak circumferential distortion in the flow controlled by autonomous bleed is associated with somewhat increased level of the steady state distortion. Although distortion remains at the low absolute levels, its increase at the highest diffuser flow rates attained in the controlled flow (that are unattainable in the uncontrolled flow due to the losses) could benefit from additional flow control devices. To illustrate the motivation behind the additional flow control approach, Figure 15 shows the two characteristic contour plots of the steady-state total pressure distributions at the AIP in the uncontrolled flow at M_{AIP} = 0.5 (Figure 15a), and in the flow controlled by the autonomous bleed (Figure 15b). As already discussed in connection with Figure 10c, the major contributor to the increased steady state distortion is the total pressure deficit region formed at the upper central surface at the AIP. This deficit is attributed to the pair of vortices that are formed by the rolled-up vorticity on either side of the upper surface, immediately upstream from the AIP (Figure 12c). Now, this was exactly a mechanism by which the two streamwise vortices formed off of the bounds of the local flow separation were inducing the total pressure deficit in the absence of the diffuser inlet cowl, i.e., when the same diffuser was integrated into the wind tunnel contraction [9]. To emphasize this point, an equivalent contour plot of the AIP total pressure for such a case is shown in Figure 15c. Clearly, the resulting pressure deficit was more pronounced in both its magnitude and spatial extent, but its form is the same; only this time realized in the weaker form due to the weaker underlying vortices. This realization led to the idea of a simple reuse of the same flow control approach which was originally designed to mitigate the total pressure deficit (and its cause of distortion) depicted in Figure 15c.

A dummy test section module, having a flush surface along the diffuser second turn, is replaced with the flow control module designed by Burrows et al. [9], which is shown schematically in Figure 16. As shown in Figure 16b, this flow control approach was designed about the local separation bubble and utilizes a spanwise array of 13 equally spaced (6.3 mm apart) fluidic oscillating jets. Each jet orifice measures 1.5 × 2 mm, with an operating frequency between f = 7 – 9 kHz over the operating range of flow rates. The jets are created by unstable interaction of two inlet streams within the body of each of the actuators and more details about this active flow control configuration are presented by Burrows et al. [9]. The jet mass flow rate coefficient C_q is considered the flow control parameter and it is defined as a ratio between the jets and diffuser mass flow rates, and in the present application is kept below 0.5%.

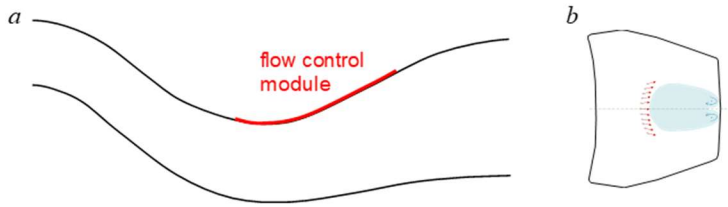

***Figure 16**. Outline of the isolated diffuser (a), and the second-turn flow control configuration (b) by [9].*

The effectiveness of this hybrid flow control when bleed of ambient air across the cowl is coupled with active fluidic control at the second turn is demonstrated at the highest diffuser flow rate, when the cowl bleed results in the highest residual time-averaged $DPCP_{avg}$. The variation of the coupled actuation is shown in Figures 17a and b for a range of actuation mass flow rates C_q. In addition, three characteristic color raster plots of the total pressure distribution at the AIP are shown in Figures 17c–e. The first important observation is that there appears to be an optimum C_q for minimization of the distortion parameter $DPCP_{avg}$. The autonomous bleed alone results in the distortion of $DPCP_{avg} = 0.022$ ($C_q = 0$). As the active flow control is activated, distortion parameter decreases continuously down to $DPCP_{avg} = 0.012$ for $C_q = 0.25\%$. This condition is also presented as a contour plot of the total pressure in Figure 17d. When comparing with the contour plot corresponding to autonomous bleed alone ($C_q = 0$) shown in Figure 17c, it is clear that the active flow control successfully suppresses the region of low pressure along the central upper surface (seen in Figure 17c). Interestingly, if the flow control parameter is increased beyond $C_q = 0.25\%$, the active flow control effect remains beneficial, but the distortion parameter increases. Analysis of the total pressure AIP contour at $C_q = 0.25\%$ (Figure 17e) indicates that the active flow control does continue to improve upon its region of effect, as the total pressure in the central upper surface continues to increase. However, a side effect of this improvement is that more of circumferential variation is created (azimuthal variation in total pressure over the AIP). These two competing effects result is somewhat less beneficial overall effect of the flow control. In addition, it is interesting to note that the total pressure recovery has a peak, regardless of how small absolute change it is, at the same optimal C_q for the distortion. Although the whole change is within 1% scale, recovery increases up to the optimum C_q, followed by the weak decrease beyond that value. Therefore, the optimum active flow control based on minimizing the circumferential distortion parameter appears to maximize recovery as well.

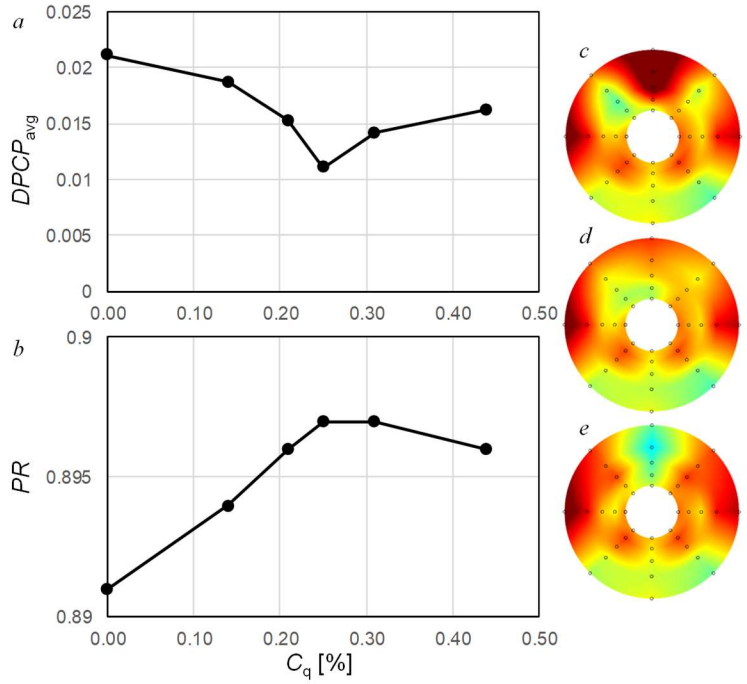

***Figure 17.** Variation of the time-averaged $DPCP_{avg}$ (a) and pressure recovery PR (b) with C_q, and corresponding color raster plots of the total pressure for $C_q = 0$ (c), 0.25% (d), and 0.45 (e) for $M_{AIP} = 0.6$.*

VII. Conclusion

The present joint experimental and numerical investigations focus on the flow through a serpentine diffuser with a cowl inlet, with an emphasis on the underlying flow structure that result in pressure losses and distortion at the diffuser's aerodynamic interface plane (AIP). The diffuser model (AIP/throat offset 0.4 D_{AIP} and $L/D = 3.7$) is installed at the intake of an open-return, pull-down, high-speed subsonic wind tunnel and its cowl inlet is integrated with a ground plane to emulate the effect of an adjacent aerodynamic surface. The CFD computational domain incorporates all the key components of the facility, and second-order-accurate solutions to the compressible Navier-Stokes equations are obtained using the Boeing's CFD finite-volume flow solver (DDES/SA-RC-QCR) employing bounded central differencing for reduced numerical dissipation and improved resolution.

The numerical simulations show that in the presence of the cowl, the flow within the diffuser is dominated by the formation and advection of a counterrotating vortex pair that forms about the center plane and two single opposite sense vortices that form at each corner. The center vortex pair moves towards the centerline and by the time they reach the second turn become unstable such that their time-averaged signature all but vanishes at the AIP while the corner vortices which are anchored by the diffuser's corners still maintain some of their coherence. High-frequency pressure measurements at the AIP and the numerical simulations show that while the unsteadiness associated with the secondary flow leads to strong instantaneous distortion, the time-averaged circumferential distortion is very low owing to the inherent flow unsteadiness and mixing. Concomitantly, the increase in total pressure losses in the presence of the cowl results in about 15% loss in recovery.

Flow losses associated with the formation of the streamwise vortices at the cowl are alleviated by disrupting their formation and interactions. This is accomplished by autonomous ingestion of ambient air into the flow over the inner surface of the cowl by exploiting the inherent pressure difference across the cowl's surface. This bleed of ambient air is achieved by a streamwise series of narrow spanwise slots across the cowl forms surface jets that introduce a layer of small-scale vorticity concentrations that disrupts the trajectories of both the central vortex pair and the corner vortices and leads to their displacements towards the center of the diffuser. The ambient air bleed across the cowl effects a large increase in recovery (to 93% from 85%) which may contribute to higher aircraft engine thrust. Furthermore, the autonomous cowl bleed lowers the peak circumferential distortion parameter $DPCP_{avg}$ by about 35% across the entire range of the present flow rates albeit with a slight increase in the time-averaged distortion owing to increased coherence at the AIP.

The control effectiveness of the ambient air bleed actuation across the cowl on the secondary vortices is augmented and enhanced by active fluidic control at the second turn of the diffuser as demonstrated earlier by Burrows et al. [9]. It is shown that while at the highest diffuser flow rate ($M_{AIP} = 0.6$), the cowl bleed alone results in a time-averaged distortion $DPCP_{avg} = 0.022$, actuation at the second turn decreases the distortion monotonically with increasing C_q, down to $DPCP_{avg} = 0.012$ (46% reduction) and while increasing the recovery to 0.897 at C_q=0.25%. These findings demonstrate the effectiveness of such hybrid, fluidic-based flow control approaches for substantial improvements in the performance of aggressive offset diffusers at takeoff and up-and-away operating conditions.

Acknowledgment

Support by an ONR Grant monitored by Dr. Steven Martens is gratefully acknowledged.

References

[1] Henne, P. "Low-speed test of translating lip axisymmetric inlets for subsonic transports," 1974.

[2] Fradenburgh, E. A., and Demarquis, D. W. "Theoretical performance characteristics of sharp-lip inlets at subsonic speeds," 1954.

[3] Fozard, J. W. "The Hawker P1127 vectored thrust fighter program - Lessons learned," *Aircraft Design, Systems and Operations Conference*. 1990.

[4] Bore, C. "Intakes for Vertical Landing Aircraft," *Practical Intake Aerodynamic Design*. 1993.

[5] Sóbester, A. "Tradeoffs in Jet Inlet Design: A Historical Perspective," *Journal of Aircraft* Vol. 44, No. 3, 2007, pp. 705-717.

[6] Hawkins, J. E. "YF-16 Inlet Design and Performance," *Journal of Aircraft* Vol. 13, No. 6, 1976, pp. 436-441.

[7] Powell, A. G., Welge, H. R., and Trefny, C. J. "Low-speed aerodynamic test of an axisymmetric supersonic inlet with variable cowl slot," *21st Joint Propulsion Conference*. Monterey, CA, 1985.

[8] Garzon, A. "Use of a Translating Cowl on a SSBJ for Improved Takeoff Performance," *45th AIAA Aerospace Sciences Meeting and Exhibit*. AIAA Paper 2007-25, 2007.

[9] Burrows, T. J., Vukasinovic, B., and Glezer, A. "Fluidic Control of an Aggressive Offset Diffuser for a Supersonic Inlet," *47th AIAA Fluid Dynamics Conference*. American Institute of Aeronautics and Astronautics, AIAA Paper 2017-4304, 2017.

[10] Mani, M., Cary, A., and Ramakrishnan, S. "A Structured and Hybrid-unstructured Grid Euler and Navier-Stokes Solver for General Geometry," *42nd AIAA Aerospace Sciences Meeting and Exhibit,* AIAA Paper 2004-524, 2004.

[11] Spalart, P. R., Deck, S., Shur, M. L., Squires, K. D., Strelets, M. K., and Travin, A. "A New Version of Detached-eddy Simulation, Resistant to Ambiguous Grid Densities," *Theoretical and Computational Fluid Dynamics* Vol. 20, No. 3, 2006, p. 181.

[12] Spalart, P., and Allmaras, S. "A one-equation turbulence model for aerodynamic flows," *30th Aerospace Sciences Meeting and Exhibit*. American Institute of Aeronautics and Astronautics, AIAA Paper 1992-439, 1992.

[13] Shur, M. L., Strelets, M. K., Travin, A. K., and Spalart, P. R. "Turbulence Modeling in Rotating and Curved Channels: Assessing the Spalart-Shur Correction," *AIAA Journal* Vol. 38, No. 5, 2000, pp. 784-792.

[14] Mani, M., Babcock, D., Winkler, C., and Spalart, P. "Predictions of a Supersonic Turbulent Flow in a Square Duct," *51st AIAA Aerospace Sciences Meeting including the New Horizons Forum and Aerospace Exposition*. American Institute of Aeronautics and Astronautics, AIAA Paper 2013-860, 2013.

[15] Winkler, C., Dorgan, A., and Mani, M. "A Reduced Dissipation Approach for Unsteady Flows on Unstructured Grids," *50th AIAA Aerospace Sciences Meeting including the New Horizons Forum and Aerospace Exposition*. American Institute of Aeronautics and Astronautics, AIAA Paper 2012-570, 2012.

[16] Marcum, D. L. "Advancing-front/local-reconnection (AFLR) unstructured grid generation," *Computational Fluid Dynamics Review* Vol. 2, 1998, pp. 140-157.